Catalysis Science & Technology

# Silver-decorated Palladium on Carbon Catalyst for Enhanced Ammonium Formate Dehydrogenation



| | |
|---|---|
| Journal: | *Catalysis Science & Technology* |
| Manuscript ID | CY-ART-07-2023-001057.R2 |
| Article Type: | Paper |
| Date Submitted by the Author: | 04-Dec-2023 |
| Complete List of Authors: | Dong, Zhun; Washington State University Gene and Linda Voiland School of Chemical Engineering and Bioengineering,<br>Mukhtar, Ahmad; Washington State University Gene and Linda Voiland School of Chemical Engineering and Bioengineering<br>Ludwig, Thomas; Lawrence Livermore National Laboratory, Materials Sciences Division<br>Akhade, Sneha; Lawrence Livermore National Laboratory, Materials Sciences<br>Hu, Wenda; Washington State University<br>Hu, Jian Zhi; Pacific Northwest National Laboratory<br>Grubel, Katarzyna; Pacific Northwest National Laboratory,<br>Engelhard, Mark; Pacific Northwest National laboratory, Environmental Molecular Sciences Laboratory<br>Wood, Brandon; Lawrence Livermore National Laboratory, Physical & Life Sciences<br>Autrey, Tom; Pacific Northwest National Laboratory, FCS<br>Lin, Hongfei; Washington State University, Gene and Linda Voiland School of Chemical Engineering and Bioengineering |
| | |

# Silver-decorated Palladium on Carbon Catalyst for Enhanced Ammonium Formate Dehydrogenation

*Zhun Dong [a], Ahmad Mukhtar [a], Thomas Ludwig [b], Sneha A. Akhade [b], Wenda Hu [a, c], Jian Zhi Hu [a, c], Katarzyna Grubel [d], Mark Engelhard [e], Brandon C. Wood [b], Tom Autrey [d], Hongfei Lin [a*]*

[a] *Gene and Linda Voiland School of Chemical Engineering and Bioengineering, Washington State University, Pullman, WA 99163, United States.*

[b] *Materials Sciences Division, Lawrence Livermore National Laboratory (LLNL), Livermore, CA 94550, United States.*

[c] *Institute for Integrated Catalysis, Pacific Northwest National Laboratory (PNNL), Richland, WA 99352, United States.*

[d] *Energy and Environment Division, Pacific Northwest National Laboratory (PNNL), Richland, WA 99352, United States.*

[e] *Environmental & Molecular Sciences, Earth & Biological Sciences, Pacific Northwest National Laboratory (PNNL), Richland, WA 99352, United States.*

**Corresponding author: hongfei.lin@wsu.edu*

**Abstract:**

Palladium (Pd)-based catalysts efficiently convert ammonium formate solution to hydrogen at low temperatures (< 100 °C), but they tend to deactivate quickly during stability testing. This manuscript presents a systematic investigation into the catalytic properties of Pd-Ag bimetallic catalysts, focusing on their surface compositions and exploring the mechanisms behind the deactivation of Pd/Ag-based catalysts. This study reports a carbon-supported Pd-Ag bimetallic nanoparticles (NPs) catalyst through a galvanic replacement method, which showed enhanced formate dehydrogenation performance. The best catalyst, Pd3Ag10/ACA-G (Pd-Ag bimetallic NPs with 3:10 mass ratio loaded on acid-washed activated carbon, prepared by galvanic replacement method), presents the highest activity with the TOF of 5202 $h^{-1}$ (~2.6-fold of commercial Pd/C). The advantages of smaller nanoparticles size with an enhanced

electron density of Pd-Ag bimetallic nanoparticles and the fact that the Ag surface alloy and Pd weakens the hydrogen adsorption energy and modulates the formate adsorption energy over the Ag/Pd (111) facet led to experimental higher turnover rates of hydrogen production. The changes on the catalyst surface, including surface Ag fraction decrease, NPs size growth, and O-containing species (carboxylate, etc.) adsorption, gradually resulted in the catalyst deactivation.

**Keywords:** Pd-Ag bimetallic catalyst; LOHCs; formate dehydrogenation; surface composition.

## 1. Introduction

Hydrogen ($H_2$) is considered a sustainable clean energy carrier that plays a vital role in the mitigation of greenhouse gas (GHGs) emissions[1–4]. In recent years, many researchers investigated the chemical storage of hydrogen using formic acid/formate salts[5–7]. The formate salt solution is considered a promising liquid organic hydrogen carrier (LOHC) with the following advantages (i) It is non-volatile, non-corrosive, non-toxic, and provides a convenient reaction medium. (ii) As reported, the Gibbs free energy changes of hydrogen release from the formate salts is close to 0 ($\Delta_rG^0 \approx 1$ kJ/mole for formate salts, $Na^+$, $K^+$, and $NH_4^+$), which makes the bicarbonate/formate-based LOHCs system thermodynamically favorable near ambient conditions[8]. (iii) Avoiding by-product CO poisoning[9,10]. Even through formic acid and formate salt have a similar molecular structure, the dehydrogenation reaction pathway and mechanism over formic acid and formate salt solution are of difference. Dehydrogenation of formic acid suffers from poisonous by-product of CO, while trace of CO was detected in the ammonium formate dehydrogenation.

Efficient dehydrogenation of a formate solution requires appropriate catalysts to generate high-purity hydrogen. Based on our previous research and others' work, the carbon-supported Pd nanoparticles show high activities for ammonium formate dehydrogenation[11]. And optimizing the support, such as removing O-functional groups[12] and introducing pyridinic/pyrrolic N species[10] on carbon, is an efficient approach to improve the Pd/C catalysts' activity for formate dehydrogenation. Besides, developing Pd-based bimetallic catalysts (Pd-Au[13–15], Pd-Ag[16–18], Pd-Ni[19], etc.) had also been investigated to enhance formate dehydrogenation reaction kinetics, among which the Pd-Ag bimetallic catalysts exhibited outstanding catalytic performance. For instance, Zhang et al. developed a composition-controlled synthesis of monodisperse 2.2 nm AgPd NPs which has high activity and stability.[20] Huang et al. reported a Pd-Ag alloy catalyst supported on the nitrogen-modified reduced graphene oxide (N-rGO) support for formic acid decomposition. The catalyst system was designed to make Pd electron-rich to enhance its utilization (The Pd and Ag atomic ratio was optimized, and the Pd1Ag6/N-rGO catalyst demonstrated a high TOF of 171 $h^{-1}$)[21]. In a similar work, Nabid et al. reported the synthesis of Ag@Pd catalyst supported on the nitrogen-modified graphene carbon nanotubes by employing Ag as a core and Pd as a shell. The catalyst was tested for formic acid decomposition, showing a TOF of 413 $h^{-1}$ at 298 K[16].

Thus far, most of the reported work on Pd-Ag systems focused on tuning the Pd/Ag ratios to optimize the formate dehydrogenation performance. In addition, Pd-Ag bimetallic alloy with a specific structure may be highly active in catalyzing hydrogen release from a formate solution. Tsang et al. prepared an Ag-Pd core-shell nanocatalyst, Ag@Pd (1:1), showing a good hydrogen generation efficiency with TOF of 500 $h^{-1}$ at

70 °C[22].

Among the several methods for the synthesis of bimetallic NPs, the galvanic replacement approach is particularly interesting due to advantages: it enables the synthesis of bimetallic hollow nanomaterials in a single reaction step with short reaction time[23]; the surface composition and morphology can be controlled by adjusting the molar ratio between the sacrificial template and the guest metal ions[24]. Galvanic replacement usually takes place between the sacrificial metal (low reduction potential) and guest metal ions (high reduction potential) in the solution[25]. However, this approach can be optimized by introducing the adsorbed hydrogen atoms. A guest metal ion with a specific reduction potential higher than hydrogen but lower than sacrificial metal could form a thin film over the sacrificial metal template but not corrode it. Thus, it is promising to generate a bimetallic catalyst with core-shell structure.

In this work, we prepare the carbon-supported Pd-Ag bimetallic NPs catalysts through the optimized galvanic replacement and co-impregnation methods. We investigate the impact of various surface compositions on formate dehydrogenation while tuning the Pd/Ag ratios to reach the highest hydrogen formation yield. The results show that the catalyst prepared by galvanic replacement with a 3:10 Pd:Ag mass ratio (Pd3Ag10/ACA-G) displayed the best dehydrogenation performance with TOF of 5202 $h^{-1}$ at 80 °C and the lowest activation energy of 33.1 kJ/mol. The characterizations are conducted to reveal the advantages of the catalyst prepared by galvanic replacement and the possible deactivation reasons hindering the application of formate-based hydrogen carriers.

## 2. Experimental section

**Materials:** The commercial Norit GSX activated carbon powder (steam activated, acid-washed) (ACA) was purchased from Alfa Aesar (L11860); Sodium hydroxide (≥98%), Ammonium formate (≥99.995%), Silver nitrate (≥99.0%) and Palladium(II) acetate (98%) were purchased from Sigma Aldrich®.

**Synthesis of Pd/ACA.** 250 mg active carbon washed by acid (ACA) support was added into 20 mL acetone, sonicating to form a uniform suspension. Then dissolve 15.8 mg Pd (II) acetate (3 wt% of Pd loading) into 20 mL acetone and mix these two suspensions. Stir till all the acetone evaporates, and then add 20 mL DI water to make a uniform suspension again. 20 mL $NaBH_4$ solution (2.22 mg/mL) was added drop by drop into the previous suspension with continuous stirring and stirred for 1 h at room temperature. After the filtration, the solids were washed with DI water and freeze-dried overnight, labeled as Pd3/ACA.

**Synthesis of Ag/ACA.** With the similar wet impregnation method, 500 mg active carbon washed by acid (ACA) support was added into 20 mL DI water, sonicating to form a uniform suspension. Then dissolve 27.4 mg $AgNO_3$ (3 wt% of Ag loading) into 20 mL DI water and mix these two suspensions. Stir at room temperature for 3 h and then add dropwise 40 mL $NaBH_4$ solution (2.22 mg/mL) into the previous suspension with continuous stirring and stir for 1 h at room temperature. After the filtration, the solids were washed with DI water and freeze-dried overnight, labeled as Ag3/ACA.

**Synthesis of PdxAgy/ACA-G.** Pd-Ag bimetallic catalysts were prepared according to the method described by Epron *et al.*[26], where Ag was deposited via the galvanic replacement reaction onto the pre-synthesized Pd/C catalyst under a reducing atmosphere according to the following reaction:

$$Ag^{+} + Pd\text{-}H \rightarrow PdAg + H^{+}$$

The as-prepared Pd3/ACA catalyst was added into 100 mL DI water (previously degassed by hydrogen bubbling) and then continuously stirred in the hydrogen flow for 2.5 h (25 °C). After that, a solution of a well-defined amount of the Ag precursor was added and maintained in contact with the suspension under hydrogen flow for another 2 h. The Pd-Ag bimetallic catalyst denoted as PdxAgyACA-G (*x* and *y* mean the mass ratio of Pd and Ag, respectively. *G* means the galvanic replacement method) was filtered, washed, and freeze-dried overnight. The schematic diagram is shown in **Figure 1**.

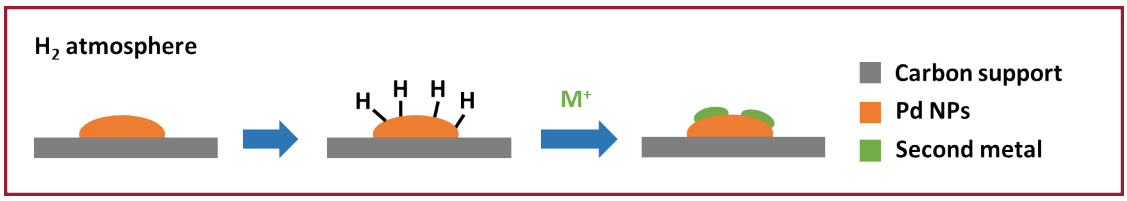


**Figure 1.** Schematic diagram of the synthesis of the Pd-based bimetallic catalysts via galvanic replacement reactions.

**Synthesis of PdxAgy/ACA-C.** The Pd-Ag bimetallic catalysts were also prepared through wet impregnation and followed by co-reduction with the $NaBH_4$ aqueous solution labeled as PdxAgy/ACA-C (*x* and *y* mean the mass ratio Pd and Ag, respectively. *C* means the co-reduction methods). Typically, Pd3Ag10/ACA-C was prepared by dispersing 500 mg ACA support into 40 mL DI water, then mixed with the Pd and Ag precursor aqueous solution (32.48 mg $Pd(NO_3)_2\ xH_2O$ and 91.25 mg $AgNO_3$ dissolving into 40 mL DI water). After magnetic stirring for 3 h at room temperature, the $NaBH_4$ aqueous solutions (231.6 mg dissolved into 40 mL DI water) were dropped into the metal precursor and ACA support mixture. After 1 h stirring at room temperature, the Pd3Ag10/ACA-C particles were collected back through vacuum

filtration, 3 times DI water washing, and freeze-dried overnight.

**Characterizations.** XPS measurements were performed using a Thermo Fisher NEXSA spectrometer with a 125 mm mean radius, full 180° hemispherical analyzer, and 128-channel detector. This system uses a focused monochromatic Al Kα X-ray (1486.7 eV) source for excitation and an electron emission angle of 60 degrees. The narrow scan spectra were collected using a passenergy of 50 eV with a step size of 0.1 eV. For the Ag 3d5/2 line, these conditions produced an FWHM of 0.84 eV ± 0.02 eV. The binding energy (BE) scale is calibrated using the Cu 2p3/2 feature at 932.62 ± 0.05 eV and Au 4f7/2 at 83.96 ± 0.05 eV. The morphology and structure of the samples were analyzed by FEI Quanta 200F field emission scanning electron microscope (SEM), JEM-2100F transmission electron microscopy (TEM) and Tecnai G2 F20 S-Twin High-revolution transmission electron microscopy (HRTEM). A Micromeritics Auto Chem II system measured the CO pulse chemisorption and temperature program decomposition. The powder X-ray diffraction (XRD) was carried out on a Rigaku Miniflex II X-ray diffractometer with 40 kV and 15 mA for CuKα (λ=0.154178 nm), with a scan range between 5~90° at the speed of 4° $min^{-1}$. The ATR-FTIR analysis was performed on the Bruker Tensor II spectrometer with Harrick Horizon Multiple Reflection ATR Accessories and a Harrick temperature controller ATC-024-4. A 2.89 mL liquid sampling cell with a ZnSe horizon trough (HON-LSP-J) was used to carry out the catalytic reactions. The *Operando* $^{13}C$ solid-state magic angle spinning (MAS) nuclear magnetic resonance (NMR) experiments were carried out using a Varian Inova wide-bore 300 MHz NMR spectrometer equipped with a 7.5 mm commercial ceramic probe. Briefly, 53 mg of catalyst and 200 uL 1M $^{13}C$ labeled sodium formate were loaded into a homemade *in situ* rotor capable of completely sealing a mixture containing solid, liquid and gaseous phases at elevated temperature and pressure[27,28]. The Larmor

frequency is 75.42 MHz and a π/4 pulse width of 3 μs with a 4 s recycle delay was used in $^{13}C$ single pulse experiments. As for $^{1}H$-$^{13}C$ cross-polarization, a π/2 pulse width of 8 μs for 1H with a 4 s recycle delay and a contact time of 1.5 ms was applied. The sample temperature was calibrated using ethylene glycol as previously reported[29].

**Dehydrogenation performance evaluation.** The formate decomposition reaction experiments were carried out in a 100 mL Parr reactor. The gas outlet was connected to a NaOH solution trap (7 M). The trap was connected to an $H_2$ digital flowmeter. The NaOH trap is used to absorb $CO_2$ generated from the bicarbonate decomposition. Before the reaction, the system was charged with $N_2$ gas 3 times to ensure no $O_2$ was in the reaction system. After the set reaction temperature was reached, the released gas was passed through the NaOH trap. Its volume was monitored using the $H_2$ digital flowmeter (M-500SCCM-D-DB9M/CM from Alicat Scientific, Inc.). The catalytic decomposition reaction for the release of hydrogen was initiated by stirring the mixture of the aqueous suspension of catalyst (0.05g) in 20 ml $NH_4HCO_2$ solution (1 M) at 80 °C after $N_2$ purging. After the dehydrogenation reaction, the spent catalyst was collected back by filtration and washed with DI water 3 times followed by freeze drying for overnight. The stability test was carried out using spent catalyst in subsequent cycles with the same process. Hot filtration experiments were conducted with the same procedure as reported before[12].

**Computational Methods.** All DFT based simulations were performed using Vienna ab initio Simulation Packages (VASP) code[30–33] with the RPBE functional[34]. Projector-augmented wave formalism[35,36] wave potentials were used for core-valence treatment. The plane-wave cutoff energy was set to 400 eV and the Brillouin zone sampling was performed with a Monkhorst-Pack k-point grid of 4×4×1. The Methfessel-Paxton scheme was used to smear the Fermi level with a Gaussian width (σ) of 0.1 eV for the

surface. Geometry optimizations were conducted with a self-consistent electronic convergence limit of $1\times10^{-6}$ eV and an ionic convergence limit of 0.05 eV $Å^{-1}$ for unconstrained atoms. DFT calculations were performed for all geometry relaxations except for computing the gas phase reference energy of hydrogen and formic acid. Periodic surface slabs of Pd(111) and Ag(111) were constructed using a 3×3 supercell with a thickness of four layers. For the Ag on Pd surface alloy (termed Ag/Pd) construction, the top layer of the 3×3×4 Pd(111) surface slab was replaced with Ag atoms. The bottom two layers of all surface slabs were held fixed at the optimized bulk lattice constant, while the top two layers were allowed to relax until convergence. Stable configuration site sampling of surface -adsorbed formate and hydrogen was performed on the surfaces. The adsorption energies of hydrogen and formate were calculated on the Pd, Ag, and Ag/Pd surfaces by evaluating the binding strength of hydrogen and formate on several high-symmetry binding sites. Hydrogen adsorption was evaluated on the three-fold face-centered cubic (FCC) and hexagonal-close-packed (HCP) hollow sites. Formate adsorption was computed with a bidentate configuration of formate wherein the formate oxygen was bound to neighboring on-top sites of Pd (Ag). Hydrogen adsorption was referenced to 0.5 $H_2$ gas. Formate ion adsorption was computed using both a thermodynamic cycle method as previously described[12] and additionally using an implicit solvent constant-potential method described below.

To mimic the effect of solution at the catalyst-liquid interface, the VASPsol implicit solvation method[37,38] was utilized to describe the solvated interface with a polarizable continuum model that treats the ions in solutions using a linearized Poisson-Boltzmann (LPB) distribution. A dielectric constant of 80 and a Debye length of 3 Å were used, corresponding to a 1 M monovalent solution, neglecting the cavitation energy contribution. The potential of zero charge (PZC) for each surface model was computed

using a constant potential calculation based on the methodology described in Duan's work[39], wherein the Fermi level was set relative to the vacuum level. The Fermi level corresponds to an applied potential value vs. the computational standard hydrogen electrode (SHE). When the net charge in the simulation cell was zero (surface charge is zero), the applied potential value obtained corresponds to the potential of zero charge ($U_{PZC}$). Adsorption energies of formate and hydrogen were recomputed at the $U_{PZC}$ value of each surface composition.

## 3. Results and discussions

### 3.1. Characterizations

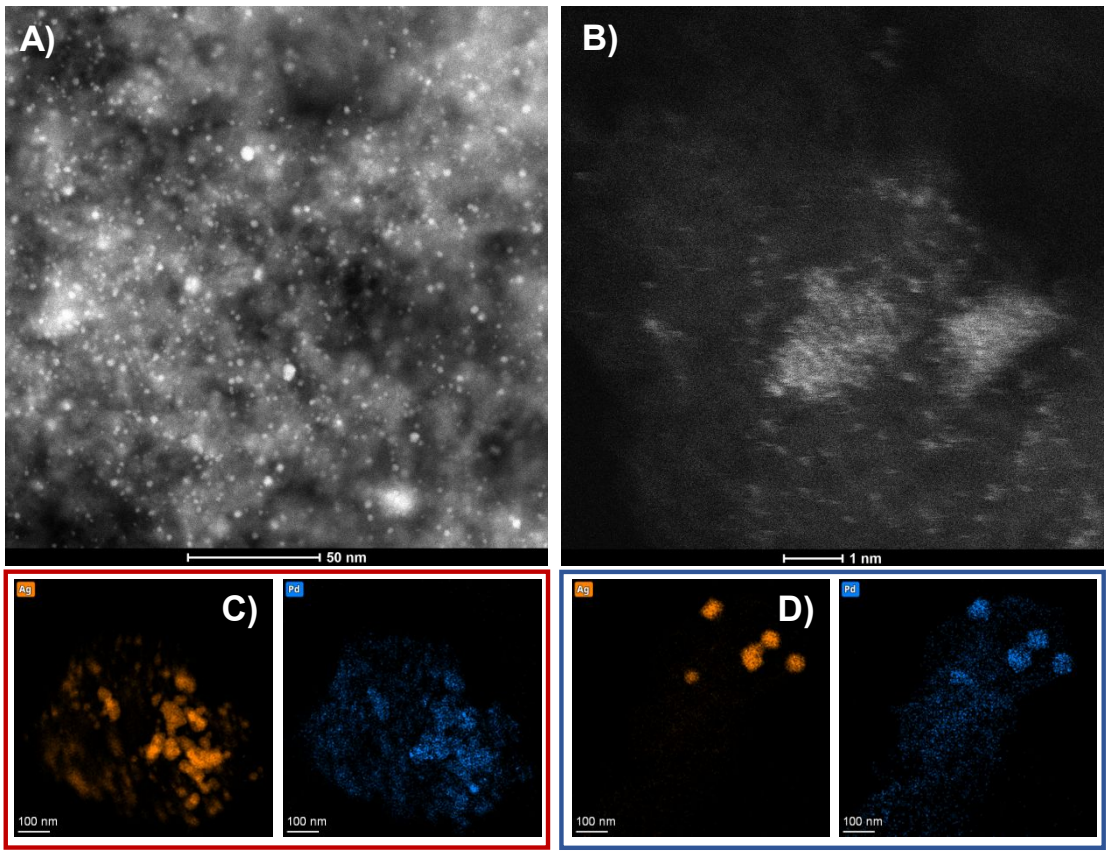


**Figure 2**. TEM images of Pd3Ag10/ACA catalysts, A-C) Pd3Ag10ACA-G; D) Pd3Ag10/ACA-C (Orange are Ag atoms and Blue are Pd atoms).

HRTEM and HAADF-STEM-mapping investigations examined the morphology, particle sizes, and composition of the Pd3Ag10/ACA-G and Pd3Ag10/ACA-C catalysts. The HRTEM images of Pd3Ag10/ACA-G shown in **Figures 2A** and **2B** reveal the Pd-Ag nanoparticles are well-dispersed on the carbon support. The mean diameter of Pd3Ag10/ACA-G is ~1.62 nm, smaller than that of Pd3Ag10/ACA-C (~2.50 nm), shown in **Figure S1**. This may be due to different formation mechanisms. The surface-decorated Ag atoms follow the morphology of small Pd NPs and would not significantly change the as-synthesized particle size, while both Pd and Ag species are more easily reduced simultaneously to form larger NPs in the co-reduction process. **Figures 2C** and **2D** display the corresponding element mapping of Pd3Ag10/ACA-G and Pd3Ag10/ACA-C, respectively. The Pd and Ag elements are homogeneously dispersed on carbon support by a galvanic replacement approach, but they are loaded with large particle size through co-reduction methods. The high-angle annular dark-field images (HAADF) of Pd3Ag10/ACA-G and Pd3Ag10/ACA-C, are shown in **Figure S2**. The lattice distance of NPs in the Pd3Ag10/ACA-G and Pd3Ag10/ACA-C are 2.21 nm and 2.36 nm assigned to Pd(111) and Ag(111), respectively. The HAADF-STEM images of the Pd5/ACA and Ag3/ACA catalysts are shown in Figure S3. For Pd5/ACA, the Pd nanoparticles were well-dispersed, and even single atoms were observed. However, the bimodal size distribution was exhibited: after statistical calculations, the small and large Pd particle sizes are within the range of 1-2.5 nm and 15-20 nm, respectively. In contrast, no single atoms were observed in the Ag3/ACA catalyst. Moreover, the Ag nanoparticles were larger and exhibited a broader size distribution with the range of 10-100 nm.

The XRD patterns of the Pd3/ACA, Ag3/ACA, Pd3Ag10/ACA-G, and Pd3Ag10/ACA-C samples were recorded to examine the crystal structures and phases, shown in **Figure**

**S4**. No noticeable peaks related to metallic Pd species could be found in the XRD pattern of Pd3/ACA, suggesting Pd NPs are highly dispersed on the carbon support. The sharp peaks at 38.1°, 44.3°, and 64.4° correspond to metallic Ag species (JCPDS No. 04-0783). The Ag peaks can be observed in Ag3/ACA, Pd3Ag10/ACA-G, and Pd3Ag10/ACA-C samples, but the peak intensities of Ag3/ACA and Pd3Ag10/ACA-C samples are higher than Pd3Ag10/ACA-G. According to the mechanism of galvanic replacement synthesis method we used in this manuscript, the Ag atoms would deposit on Pd NPs surface, and replace the adsorbed H atoms to form a microstructure that Pd NPs surface decorated with Ag atoms. Therefore, the Pd-Ag alloy particle size should be very similar with the original small Pd particle size, which is too small to show a clear diffraction peak in the XRD pattern. The Ag (111) peak shown in the **Figure S4** is related to excessive Ag precursor, which is reduced to form metallic Ag NPs loaded on the carbon support.

The XPS analysis reveals that the Pd3Ag10/ACA-G and Pd3Ag10/ACA-C catalysts contain C, O, Pd, and Ag elements without other significant impurities shown in **Figure S5A**. **Table 1** summarizes surface element atomic fractions, indicating that the Pd3Ag10/ACA-G has a higher surface Ag concentration (6.00% vs. 2.31%) but lower Pd fractions (0.62% vs. 3.65%) compared with Pd3Ag10/ACA-C. The atomic ratio of Pd and Ag was 1.6 when we synthesized Pd3Ag10/ACA-C through the co-reduction method. However, the galvanic replacement efficiently decreases the surface Pd/Ag atomic ratio from 1.6 to 0.1. Thus, most Pd species were decorated with Ag atoms after galvanic replacement. Besides, the O atomic fractions of Pd3Ag10/ACA-C and Pd3Ag10/ACA-G are 5.74% and 6.25%, respectively.

In the Pd 3d spectra (**Figure 3A**) of Pd3Ag10/ACA-C and Pd3Ag10/ACA-G, two main peaks associated with metallic Pd(0) 3d5/2 and Pd(0) 3d3/2 are located at 335.9 eV and 341.1 eV, respectively. Two peaks at higher binding energies (337.6 eV and 342.6 eV) correspond to the Pd(II) species[40,41]. The peaks at 344.3 eV in both samples are related to the satellite structure highly correlated to the electrons in the partially filled *d* orbitals[42]. The Pd(0)/Pd(II) ratios in both samples were calculated using the peak areas of Pd $3d_{5/2}$. The Pd3Ag10/ACA-C has a higher Pd(0)/Pd(II) ratio of 2.62 compared with Pd3Ag10/ACA-G (1.15), suggesting Pd(II) ions consist of surface Pd species. In other words, the Ag atoms are favorable to deposited on the metallic Pd surface due to no adsorbed H on Pd(II) surface, which confirms the galvanic replacement mechanism (shown in **Figure 1**) that Ag(I) ions replace the adsorbed H over Pd surface to form Ag(0) atoms. Besides, the exact Pd(II) $3d_{5/2}$ binding energy of Pd3Ag10/ACA-G is 337.4 eV, lower than that of Pd3Ag10/ACA-C (342.6 eV). More electrons were transferred to Pd(II), resulting in Pd(II) species of Pd3Ag10/ACA-G being electron-rich. The Pd(0) $3d_{5/2}$ binding energy of Pd3Ag10/ACA-G is close to but slightly lower than that of Pd3Ag10/ACA-C (335.7 eV vs. 335.9 eV). It indicates that metallic Pd species are in a similar surface condition, but metallic Pd species over Pd3Ag10/ACA-G also represent trend to enriched electrons.

In the Ag 3d spectra (**Figure 3B**) of Pd3Ag10/ACA-G, two main peaks at 368.4 eV and 374.4 eV are assigned to metallic Ag species[43,44]. No Ag(I) related peaks were observed, all the Ag species are in metallic states. In comparison, the Ag(0) 3d peaks of Pd3Ag10/ACA-C shift to lower binding energy 368.2 eV and 374.2 eV, respectively,

which is the opposite of the binding energy shift trend in the Pd 3d spectra (**Figure 3A**). As shown in **Table 1**, the surface Ag/Pd ratio of Pd3Ag10/ACA-G is 9.68, ~15-fold higher than that of Pd3Ag10/ACA-C (0.63). Like the report of Mustafa et al., the core-level shifts in the binding energy of Ag $3d_{5/2}$ showed a good linear relationship with the number of Pd atoms neighbors around Ag atoms. Higher binding energies correspond to more contiguous Ag ensembles with a lower number of Pd neighbors per Ag atom[45]. In our case, more contiguous Ag atoms are formed on the Pd3Ag10/ACA-G surface, leading to the Ag $3d_{5/2}$ peak shifting to higher binding energies.

In the high-resolution XPS spectra of O 1s (**Figure S5B**), the asymmetric peaks suggest different forms of $O^{2-}$ existing in Pd3Ag10/ACA-C and Pd3Ag10/ACA-G. The peaks at 532.1 eV and 533.4 eV are assigned to the C-O bonds of adsorbed hydroxyl groups on the carbon support and -OH of hydroxyl groups, respectively. Moreover, the broad adsorbed oxygen peaks were detected at 537.4 eV. The same binding energy of C-O bonds and O-H bonds of hydroxyl groups and similar O fractions of Pd3Ag10/ACA-G and Pd3Ag10/ACA-C samples suggest the O-containing groups are not significantly changed during co-reduction and galvanic replacement methods.

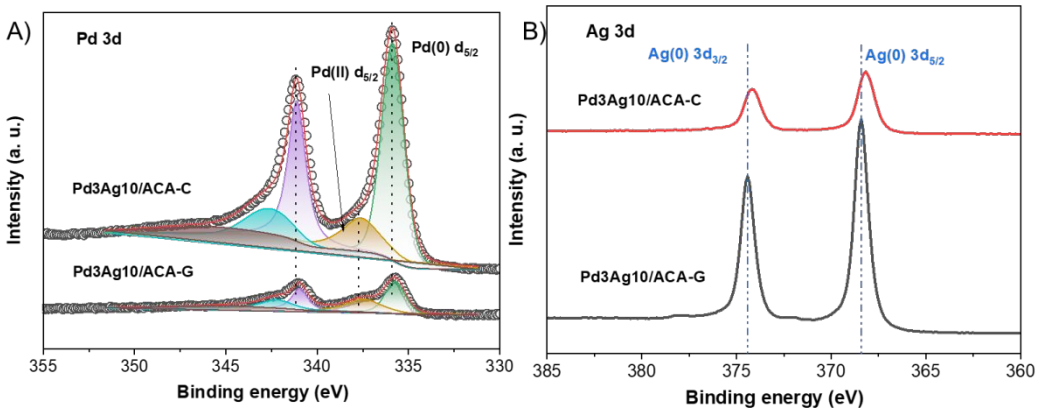


**Figure 3**. A) Pd 3d, B) Ag 3d XPS spectra of Pd3Ag10/ACA-C and Pd3Ag10/ACA-G.

**Table 1.** Surface elements containing in Pd3Ag10/ACA-C, Pd3Ag10/ACA-G, and Spent Pd3Ag10/ACA-G.

| Catalyst | Surface elements atomic fraction | | | |
|---|---|---|---|---|
| | C (%) | O (%) | Pd (%) | Ag (%) |
| Pd3Ag10/ACA-C | 88.30 | 5.74 | 3.65 | 2.31 |
| Pd3Ag10/ACA-G | 87.12 | 6.25 | 0.62 | 6.00 |
| Spent Pd3Ag10/ACA-G | 88.94 | 7.12 | 0.85 | 3.09 |

## 3.2. Activity evaluations

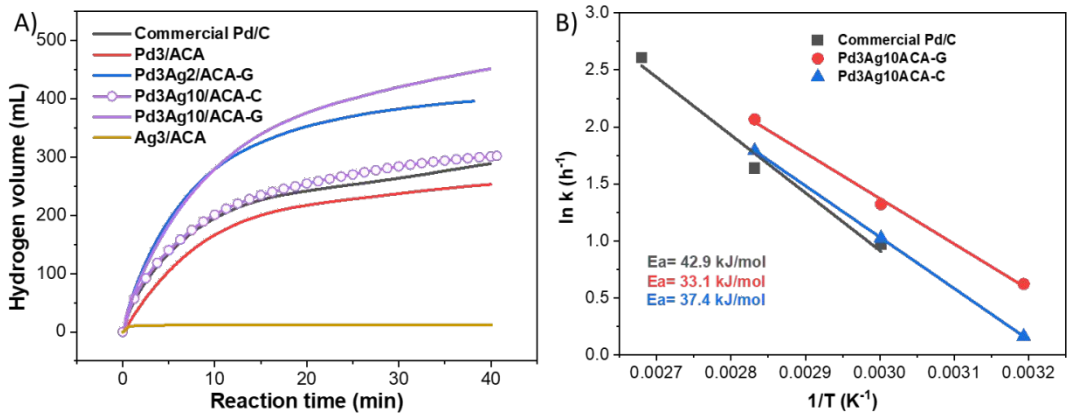


**Figure 4**. Formate dehydrogenation performance over A) Pd-Ag catalysts with increasing Ag ratios and Pd-Ag catalysts with different structures. Reaction conditions: 0.05 g catalyst, 20 mmol Ammonium formate, 80 °C, 40 min, 1 atm N2. B) Kinetics of Arrhenius plots over Pd3Ag10/ACA-G, Pd3Ag10/ACA-C, and commercial Pd/C (the initial reaction rates were averaged from 0 to 5 min).

To investigate the catalytic performance of formate dehydrogenation over Pd-Ag bimetallic nanoparticles supported on carbon support catalysts, we evaluated the activities of the Pd-Ag/ACA catalysts with different Pd/Ag ratios. **Figure S6** shows that only a trace amount of $CO_2$ and no ammonia were detected in the gas phase products. Contrarily, hydrogen is the dominant gaseous product and accounts for 99.6

v% (**Table S1**). As shown in **Figure 4A**, under the same reaction conditions (0.05 g catalyst, 20 mL 1 M ammonium formate, 80 °C, 1 atm of $N_2$, 40 min), the released $H_2$ volumes (or $H_2$ yields) over the Pd3/ACA, Pd3Ag2/ACA-G, Pd3Ag10/ACA-G, and Ag3/ACA catalysts are 253 mL (50%), 396 mL (79%), 451 mL (90%), and 12 mL (2%), respectively. The hydrogen volume over Pd3/ACA monometallic catalyst is lower than that of the commercial Pd/C (5 wt% Pd loading) (288 mL $H_2$ or 57% yield of $H_2$) due to a lower Pd loading. However, both Pd-Ag/ACA-G catalysts have improved hydrogen yields over commercial Pd/C even though with lower Pd loading. It suggests that surface-decorated Ag can significantly facilitate dehydrogenation performance. With an increasing amount of Ag species introduction, the hydrogen yields enhanced from 78.6% to 89.5%, further confirming the specific contribution of surface-decorated Ag species. Ag3/ACA catalyst generates little hydrogen (12 mL, 2%) compared with other Pd-based catalysts, demonstrating that the metallic Ag nanoparticles are not the active sites of formate dehydrogenation. Thus, when more surface-decorated Ag species were added, the interaction between Pd-Ag species was enhanced, leading to higher activity instead of adding more active sites. Therefore, attention should be paid to studying Pd-Ag interaction to understand the mechanisms of Pd-Ag catalysts efficiently converting formate to bicarbonate.

To gain more insight into the Pd-Ag species interactions, we evaluated the formate dehydrogenation performance over Pd3Ag10/ACA-G and Pd3Ag10/ACA-C at the same reaction conditions (**Figure 4A**).After 40 minutes, the Pd3Ag10/ACA-G catalyst shows a higher hydrogen yield (451 mL, 90%) than Pd3Ag10/ACA-C (301 mL, 60%) and Pd3/ACA (253 mL, 50%), indicating that both kinds of Pd-Ag bimetallic active sites are more beneficial to monometallic Pd active sites, following an efficiency order

that Pd-based surface decorated structure > bulk alloy structure > monometallic active site. As shown in **Table 2**, the Pd3Ag10/ACA-G has a 2.6-fold higher turnover frequency (TOF, the detailed TOF calculation is shown in Supporting Information) of 5202 $h^{-1}$ than the commercial Pd/C (1966 $h^{-1}$). The TOFs of the Pd3Ag10/ACA-C and Pd3/ACA are 3395 $h^{-1}$ and 2804 $h^{-1}$, respectively, suggesting that the Pd-Ag bimetallic structure plays a more vital role than the composition ratio. Indeed, the Pd3Ag10/ACA-G has a higher TOF than most Pd-Ag-based catalysts reported in the literature under comparable reaction conditions (**Table 2**). Zhao et al.[46], Yin et al.[47], Song et al.[48], and etc. calculated TOF per unit of the total amount of loaded metal species. In this report, Ag species have no activity for formate dehydrogenation. Thus, we calculated the TOF based on the total amount of Pd loading. The catalysts with the reported TOF (turnover frequency) data are labeled with various superscripts to distinguish the different TOF calculation methods. Our as-developed Pd3Ag10/ACA-G displayed enhanced TOFs compared with most reported Pd-Ag bimetallic catalysts, as shown in Table 2. For instance, Yin et al.[47] mentioned the TOF, based on total metal loading, of $Pd_{0.7}Ag_{0.3}/CeO_x$-NPC was 875 $h^{-1}$ in dehydrogenation of the formic acid and sodium formate mixture. It was revised to 1250 $h^{-1}$ when calculated through the same method as we used, i.e., normalized by the Pd loading amount, which is still lower than that of Pd3Ag10/ACA-G (1790 $h^{-1}$) at 40 °C. An exception is Masuda et al.[49] reported $TiO_x$ shell-modified core−shell Ag@Pd supported on $TiO_2$, which exhibited a high TOF of 6499 $h^{-1}$ at 75 °C, calculated over the total amount of Pd loading. The presence of Ag sites and $TiO_x$ shell in the vicinity of Pd likely promoted the rate-limiting C−H bond dissociation step during dehydrogenation. Nevertheless, the Pd3Ag10/ACA-G catalysts are easily utilized in practical applications due to their robust structure and relatively simple synthesis method compared to the $TiO_x$ shell-modified core-shell Ag@Pd

catalysts.

It is interesting to compare the dehydrogenation of ammonium formate (AF), formic acid (FA), and their mixtures (AF + FA) over the Pd3Ag10/ACA catalyst. We found that FA dehydrogenation alone was slower than that of AF under identical reaction conditions (Figure S7). Considering the mixture of AF and FA (50:50), the dehydrogenation of AF was adversely affected by FA in terms of the overall $H_2$ yields. It is not surprising that the dehydrogenation of AF yielded ammonium bicarbonate and hydrogen ($HCOO^- + H_2O \rightarrow HCO_3^- + H_2$) with the Pd3Ag10/ACA catalyst. However, ammonium bicarbonate further reacted with FA in the solution to be converted back to AF and co-produce $CO_2$ ($HCO_3^- + HCOOH \rightarrow HCOO^- + H_2O + CO_2$). The presence of $CO_2$ might inhibit AF dehydrogenation as both FA and AF/FA dehydrogenation yielded only approximately 50% of $H_2$ from AF dehydrogenation after 40 minutes of the reactions. This phenomenon should be further investigated.

The kinetic rate measurements of as-developed Pd3Ag10/ACA-G, Pd3Ag10/ACA-C, and commercial Pd/C were conducted at 40 °C -100 °C, as shown in **Figure S8**. The calculated TOFs of Pd3Ag10ACA-G from 40 °C to 80 °C increased from 1799 $h^{-1}$ to 5202 $h^{-1}$, indicating higher reaction temperatures benefits the dehydrogenation kinetics. The corresponding Arrhenius plots were obtained according to the first-order power law kinetic model[12] and were shown in **Figure 4B**. The activation energies ($E_a$) of Pd3Ag10/ACA-G and Pd3Ag10/ACA-C were 33.1 kJ/mol and 37.4 kJ/mol, lower than that of commercial Pd/C (42.9 kJ/mol). It means the formate dehydrogenation can be performed with a lower energy barrier over Pd-Ag bimetallic active surface, in which the one prepared by galvanic replacement is more favorable than the one prepared by the co-reduction method.

**Table 2.** The catalytic activity of different Pd-Ag based catalysts for the formate dehydrogenation.

| **Catalysts** | **Substance** | **T (°C)** | **TOF ($h^{-1}$)** | **Ref.** |
|---|---|---|---|---|
| Commercial Pd/C | $NH_4HCO_2$ | 80 | 1966 [a] | |
| Pd3/ACA | $NH_4HCO_2$ | 80 | 2804 [a] | |
| Pd3Ag10/ACA-C | $NH_4HCO_2$ | 80 | 3395 [a] | This work |
| Pd3Ag10/ACA-G | $NH_4HCO_2$ | 80 | 5202 [a] | |
| | | 40 | 1790 [a] | |
| PdAg/rGO | $H_2CO_2/NaHCO_2$ | 25 | 164 [b] | 46 |
| $Pd_{0.7}Ag_{0.3}$/CeOx-NPC | $H_2CO_2/NaHCO_2$ | 30 | 875 [b] | 47 |
| PdAg@$ZrO_2$/C/rGO | $H_2CO_2/NaHCO_2$ | 60 | 4500 [b] | 48 |
| PdAg-MnOx/N-$SiO_2$ | $H_2CO_2$ | 25 | 1430 [b] | 50 |
| C-PdAg BNSs | $H_2CO_2/NaHCO_2$ | 50 | 378 [b] | 51 |
| PVPI@PdAg NWs | $H_2CO_2$ | 25 | 312 [b] | 52 |
| Ag@Pd@TiOx(TTIP)/$TiO_2$ | $NaHCO_2$ | 75 | 6499 [a] | 49 |
| PdAg/CN-3% | $H_2CO_2$ | 30 | 254 [b] | 53 |

* TOF was calculated based on different sites. a: based on total Pd atoms; b: based on total metal atoms;

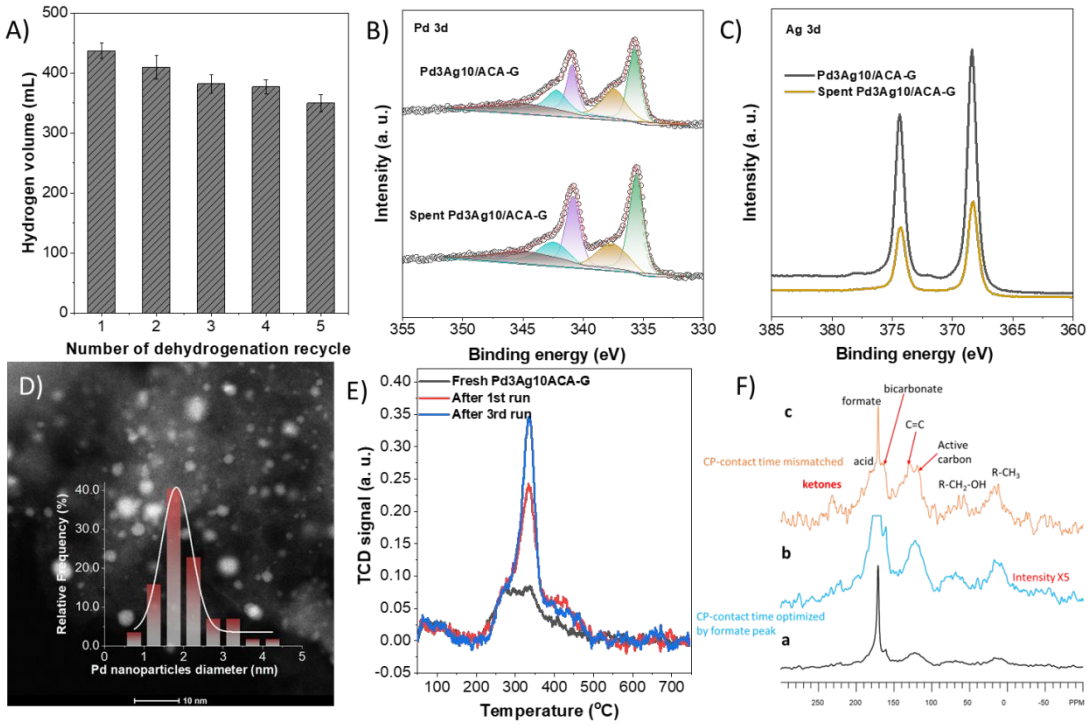


**Figure 5**. A) recyclability of Pd3Ag10/ACA-G (Reaction conditions: 0.05 g catalysts, 20 mmol ammonium formate, 80 °C, 1 atm N2, 40 min). B) Pd 3d; C) Ag 3d XPS spectra comparison of fresh and spent Pd3Ag10/ACA-G. D) HRTEM image of spent Pd3Ag10/ACA-G and NPs size distribution (inset). E) TPD curves of fresh and spent Pd3Ag10/ACA-G after different cycles. F) $^{1}H$-$^{13}C$ cross-polarization NMR spectra of formate decomposition over Pd/Ag/AC catalyst (a) optimized CP condition with respect to the formate peak (full intensity spectrum); (b) vertically expanded by 5 times of (a); (c) mismatched conditions with respect to formate but more matched for the other peaks.

In addition, the stability tests were performed using the recycled Pd3Ag10/ACA-G catalysts (**Figure 5A**). We observed that the activities gradually decreased during the formate dehydrogenation reactions throughout five repeated cycles. The TOFs at different cycles were calculated and summarized in Table S3. Similar with the total hydrogen volume decrease, the TOFs calculated by first 10 min data gradually reduce from 5202 $h^{-1}$ to 3242 $h^{-1}$, indicating a intrinsic deactivation occurs over

Pd3Ag10/ACA-G catalyst. In parallow, other researchers reported the deactivation of Pd-Ag bimetallic catalysts, as well. Zhao et al, demonstrated the Pd0.9Ag0.1B/rGO lose obvious activity in the third run, which was attributed to the aggregation of rGO during the reaction process[46]. Yang et al, reported the AgPd NPs were well dispsered on the graphene without no obvious agglomeration but the catalytic actvitiy slightly decreases in the third run[54]. Multiple possible reasons make it unclear to account for deactivation. Herein, a systematic investigation of deactivation mechanism was conducted to have a insight on that. The ICP-MS analysis of the spent Pd3Ag10/ACA-G (**Table S4**) and the hot filtration experiment (**Figure S9**) revealed no Pd leaching during the reaction. The XPS spectra of the spent Pd3Ag10/ACA-G were compared with the fresh Pd3Ag10/ACA-G to elucidate the possible deactivation mechanism. The Pd 3d spectra (**Figure 5B**) display that the metallic Pd species of spent Pd3Ag10/ACA-G maintain the same binding energy as fresh Pd3Ag10/ACA-G, indicating Pd species are stable during dehydrogenation. And the Pd(0)/Pd(II) ratio of the spent catalyst is 2.08, higher than that of the fresh catalyst (1.15), demonstrating more Pd(II) species were reduced to the metallic state, which would be beneficial to keep high activity. The Ag 3d spectra of the spent catalyst (**Figure 5C**) show the same binding energy but a lower peak intensity, meaning the Ag electronic conditions are stable, but the quantity of Ag species decreases. **Table 1** reveals the specific Pd and Ag atomic fraction changes after dehydrogenation. The Pd fractions increase from 0.62% to 0.85%, while the Ag fractions decrease from 6.00% to 3.09%. It means the surface structure is reconstructed after the reaction, around half of Ag species leave from the surface decorated Pd-Ag nanoparticles, and a little more Pd are explored. This surface structure change possibly led to deactivation due to the Pd monometallic NPs support on carbon showing a relatively low activity. As shown in **Figure 5D**, the HRTEM image of the spent

Pd3Ag10/ACA-G catalyst present means Pd NPs size is 2.00 nm, larger than that of fresh catalyst (1.62 nm). The slight growth of Pd NPs size may also be one of the deactivation reasons. **Table S4** showed that the Pd dispersion tested by CO pulse chemisorption of Pd3Ag10/ACA-G decreases from 21.4% to 19.2% and 17.9% with the cycling reaction. It is attributed to the larger NPs size tested by HRTEM and occupation of chemically bonded carboxylate species tested by TPD. TPD spectra of fresh and spent catalysts after different cycles are shown in **Figure 5E**. Compared with fresh Pd3Ag10/ACA-G, two peaks at 335 °C and 420 °C appear after one-time dehydrogenation. After a three-cycles reaction, the peak at 335 °C increased further, while the peak at 420 °C maintains the same peak intensity. According to our previous research, the multiple O-containing species on the carbon support will decompose during the temperature ramping. The carboxylate species decompose from 250 °C to 350 °C, and the lactone species decompose from 350 °C to 450 °C. The adsorbed carboxylate species are dominant component negatively impact the formate dehydrogenation activity. On the Pd3Ag10/ACA-G surface, carboxylate related species with 335 °C decomposition temperature, accumulate on the catalyst surface with more cycle's operation, high possibly leading to the deactivation. Besides, it is well accepted that Pd NPs are mobile and unstable on the carbon surface, resulting in aggregation and change of surrounding bonding conditions during the reaction, which may lead to deactivation. Therefore, multiple factors, such as the surface decorated Pd-Ag nanostructure change, growth of NPs size, and intermediate poisoning adsorption, lead to the deactivation of Pd3Ag10/ACA-G in the formate dehydrogenation reaction. In addition, to further unravel the origin of deactivation, the *Operando* NMR $^{1}H$-$^{13}C$ cross-polarization was employed to identify surface-adsorbed species, shown in **Figure 5F**. By optimizing the contact time of cross-polarization with regard to the formate

resonance, the formate peak at 171 ppm displays the highest intensity. Other relatively lower peaks are observed clearly as well by expanding the spectrum five times. By mismatching the optimized conditions, besides formate and bicarbonate peaks, those small peaks are still observable, including other minor visible peaks. These peaks between 220-240, 180-190, 100-140, 50-90, and 0-30 ppm are attributed to ketones, acid, C=C, oxygenated carbon, and aliphatic carbon, respectively[55]. They are tightly bound on the surface such that $^{1}H$-$^{13}C$ cross-polarization can catch these resonance signals, evidencing that these surface-adsorbed carbon species are responsible for the fast deactivation. Based on the signature peaks associated with ketones, acid, C=C, oxygenated carbon, and aliphatic carbon, a model of, likely a large molecule containing the identified functional groups by NMR, should be able to be proposed to describe the surface adsorbed chemical species that are responsible for the catalyst deactivation.

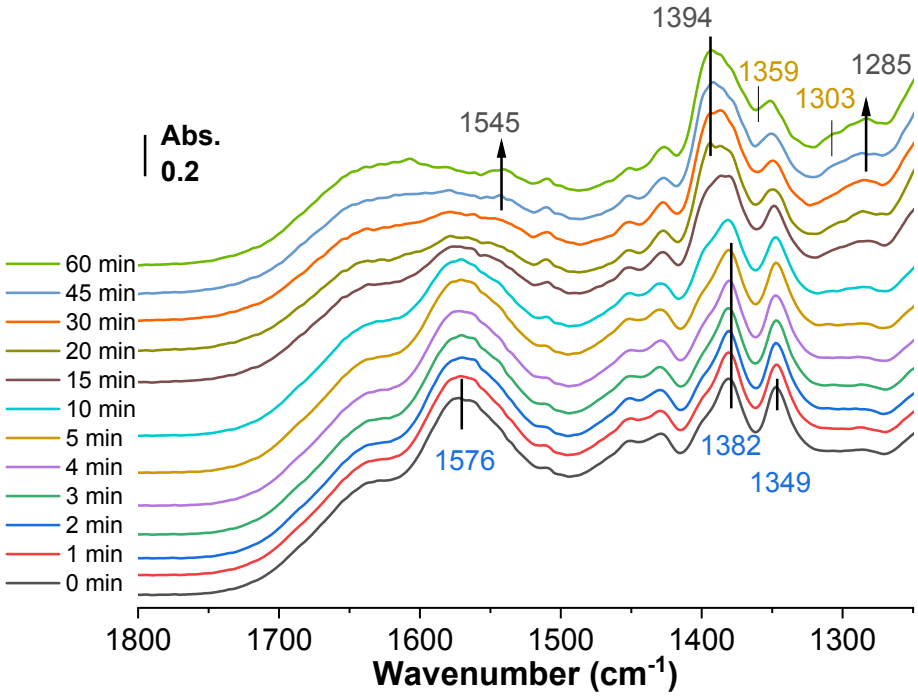


**Figure 6**. Selected *in-situ* ATR-IR spectra on Pd3Ag10/ACA-G catalyst at 40 °C as a function of time recorded after rinsing a 2 M ammonium formate solution to the spectral cell.

The reference spectrum was recorded in the air before the rinse.

The *in-situ* ATR-IR of formate dehydrogenation over Pd3Ag10/ACA-G catalyst to further understand the ammonium formate dehydrogenation mechanism, enabling the time-resolved monitoring of formate conversion and bicarbonate formation. The formate-specific bands are at 1576, 1382, and 1349 $cm^{-1}$, while the peaks at 1359 and 1303 $cm^{-1}$ are related to bicarbonate bond vibrations[12]. **Figure 6** shows the selected *in-situ* ATR-IR spectra recorded in the air at 40 °C for 1 h of the formate conversion on the Pd3Ag10/ACA-G catalyst. (The *in-situ* ATR-IR tests at different temperatures are shown in **Figure S10**.) At the initial stage, the specific peaks of formate can be observed at 1576 $cm^{-1}$, 1382 $cm^{-1}$, and 1349 $cm^{-1}$ after the catalyst film is rinsed by a 2 M ammonium formate aqueous solution. Then the formate peaks at 1576 $cm^{-1}$ and 1382 $cm^{-1}$ decreased significantly after 15 min of reaction, while the bicarbonate peaks at 1353 $cm^{-1}$ are so weak to be overlapped by formate peaks at 1349 $cm^{-1}$, and the bicarbonate peaks at 1303 $cm^{-1}$ are also barely to be ignored. Interestingly, a new peak at 1545 $cm^{-1}$ is related to carbonate, one possible intermediate of formate dehydrogenation to bicarbonate. Besides, two new peaks are enhanced during the dehydrogenation at 1394 $cm^{-1}$ and 1285 $cm^{-1}$, which are assigned to carboxylate species symmetric stretching. This result is consistent with the TPD peak at 335 °C shown in **Figure 5E**, further confirming that the intermediate carboxylate species are generated from formate but strongly adsorbed on the catalyst surface and poisoned the surface-active site. In addition, the *Operando* $^{13}C$ single pules NMR of formate decomposition over the Pd3Ag10/ACA-G catalyst was operated to study the reaction mechanism. The reaction was taken as the temperature increases, shown in **Figure S11**. The dominating peaks observed at about 171 ppm are ascribed to formate reactant, while the increasing

peak at 160 ppm with temperature is assigned to bicarbonate product[56]. The fact that bicarbonate is generated at such a sluggish pace at even 93 °C reveals that there is a severe deactivation occurring during the operando NMR study in the spinning rotor. As the intensity vertically is enlarged by 20 times, the $CO_2$ peak at 125 ppm is clearly observed during the operando study[57]. However, when comparing intensities of bicarbonate and $CO_2$, it is evident that the product bicarbonate is a very stable species under this environment, with only less than 3% of bicarbonate decomposing to $CO_2$.

### 3.3. Computational results

To examine the role of Ag in the Pd-based catalyst for formate dehydrogenation, the energies of hydrogen and formate adsorption on Pd (111), Ag (111), and Ag/Pd (111) surfaces were computed using first-principles DFT calculations. The representative structures for optimized configurations of adsorbed formate and hydrogen are displayed in **Figure 7**. Model selection was based on the XPS results which showed that the Ag surface fraction (6.00 %) was 10 times higher than Pd surface fraction (0.62 %) of the as-prepared Pd3Ag10/ACA-G. Thus, the Ag/Pd surface was constructed as a surface alloy of Pd (111) with an Ag on-top layer, as shown in **Figure 7**.

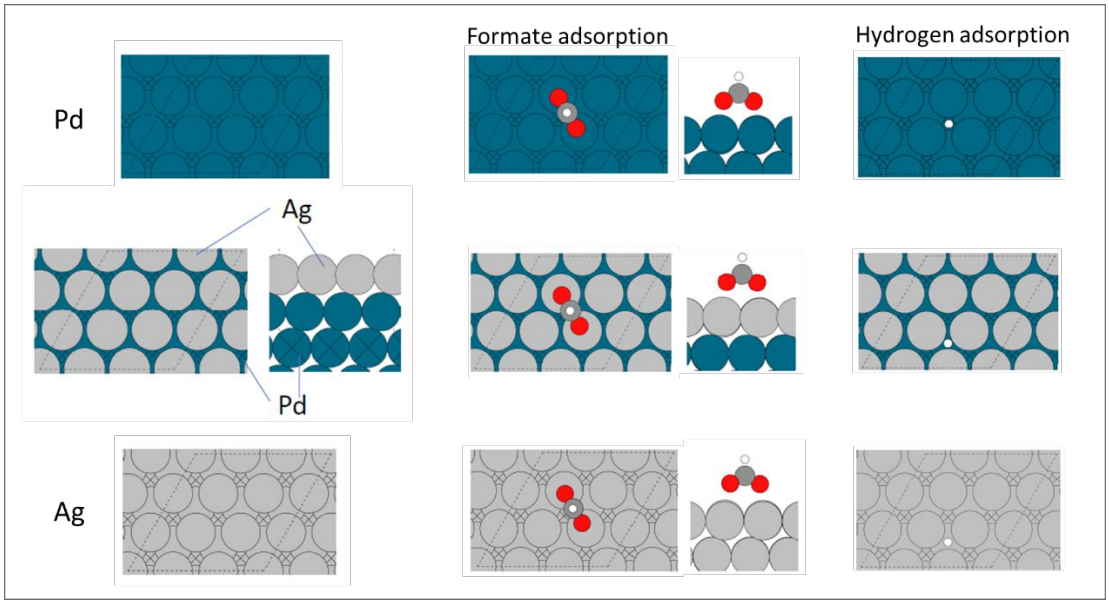


**Figure 7.** View of Pd (111), Ag (111), and Ag/Pd (111) surface alloy models, and the representative configurations for formate and hydrogen bound to positions of Pd, Ag, and Pd-Ag bimetallic surface. Atom color representations: Pd (teal), Ag (grey), O (red), C (dark gray), and H (white).

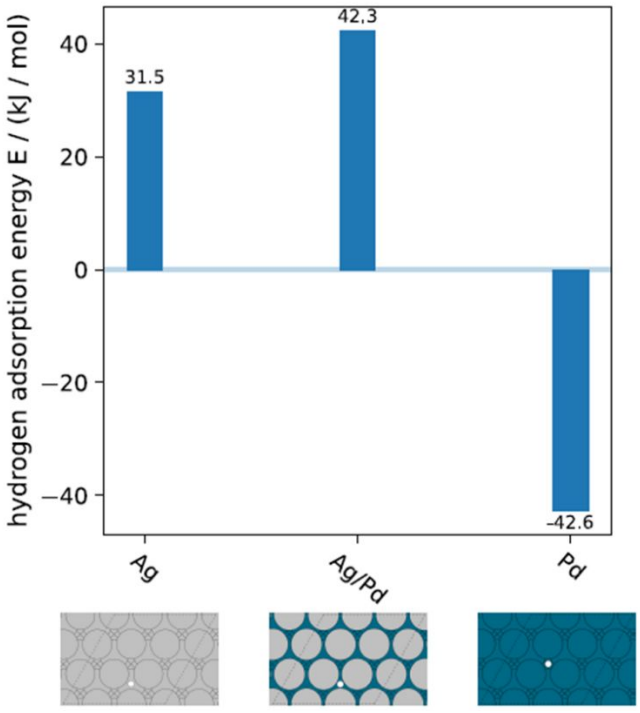


**Figure 8**. Adsorption energies (in kJ/mol) of hydrogen on Ag (111), Ag/Pd (111) and Pd (111) surfaces. Atom color representations: Pd (teal), Ag (gray), O (red), C (dark gray) and H

(white).

**Figure 8** shows the adsorption energies of hydrogen on the different surface models. The hydrogen adsorption energy on Pd (111) surface is -42.6 kJ/mol, much lower than Ag (111) surface (31.5 kJ/mol) indicating strong binding of hydrogen to Pd compared to the Ag surface. The binding is further weakened on Ag/Pd (42.3 kJ/mol) indicating that the electronic and compressive strain on Ag overlayer (lattice constant Ag ~ 4.09 Å, Pd ~ 3.89 Å) in the Ag/Pd surface can play an important role in tuning the binding energy of hydrogen and formate. **Figure 9** further highlights the synergistic effect of Ag and Pd on formate binding. **Figures 9A** and **9B** show the influence on the binding energy with inclusion of solvation and potential considerations in the calculations. When solvation and potential of zero charge (PZC) are accounted for (**Figure 9B**), the formate adsorption is much stronger on Pd (111) surface (-88.9 kJ/mol) and weaker on Ag (111) surface (-21.3 kJ/mol). The formate adsorption strength is intermediate on the Ag/Pd surface alloy (-42.6 kJ/mol). This trend can be primarily rationalized by the potential of zero charge $U_{PZC}$ of these surfaces that is intrinsically linked to the surface charge transfer coefficient and modulated by the catalyst composition, adsorbed species, and the microenvironment at the catalyst/solution interface. **Figure S12** shows the computed $U_{PZC}$ of Ag is -0.62 V vs. SHE, lower than that of Ag/Pd surface alloy (-0.50 V vs. SHE) and Pd surface (0.24 V vs. SHE); consistent with previously published results[58,59]. The higher $U_{PZC}$ value of Pd intrinsically makes Pd have a higher affinity towards negatively charged adsorbates like formate ions relative to Ag. The $U_{PZC}$ of Ag/Pd is lower than Pd and plays a critical role in modulating the strength of formate adsorption. While the capacitance effect shown here will likely weaken as the coverage of formate increases, the results in **Figure 9B** and **Figure S12** highlight the electronic role of the metal/liquid interphase in modulating catalytic events such as adsorption and

dehydrogenation. Following Sabatier's principle, we rationalize that the temperate bonding strength between the formate reactant and catalytic active site results in a higher TOF and enhanced dehydrogenation performance as observed experimentally with Pd3Ag10/ACA-G. Additionally, weak hydrogen binding on the Ag/Pd surface alloy can promote associative desorption of $H_2$ from the catalyst surface.

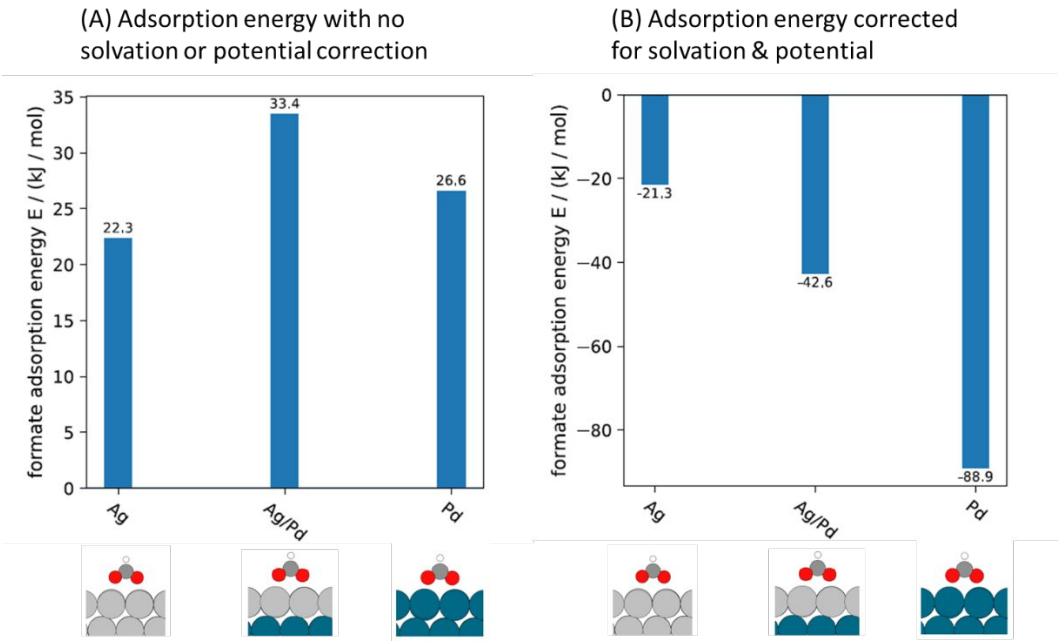


**Figure 9.** Adsorption energies (in kJ/mol) of formate on Ag (111), Ag/Pd (111) and Pd (111) surfaces (A) without and (B) solvation and potential correction. Adsorption energies in (A) use a vacuum/metal interface. Energies in (B) use 1 M monovalent equivalent implicit solution with the surface set at its $U_{PZC}$ (net surface charge = 0). Atom color representations: Pd (teal), Ag (gray), O (red), C (dark gray) and H (white).

### 3.4. Catalyst structure-performance discussion

According to the formate dehydrogenation evaluations (**Figure 4A**), the Pd-Ag bimetallic catalysts prepared by galvanic replacement method, Pd3Ag2/ACA-G and Pd3Ag10/ACA-G, displayed improved hydrogen production (396 mL and 451 mL) compared to monometallic catalyst Pd3/ACA (253 mL). However, the hydrogen

production increased from 253 mL to 396 mL (56.5 % improvement) only with 2 wt% Ag atoms doping, while that increased from 396 mL to 451 mL (12.2 % improvement) with the Ag loading increased from 2 wt% to 10 wt%. It means that the existence of the Pd surface decorated with Ag atoms can significantly improve the formate dehydrogenation performance. DFT simulations further substantiate the role of surface Ag in decreasing the electron affinity of Pd thereby weakening the hydrogen adsorption energy (**Figure 8**) and modulating formate binding with intermediate adsorption strength (**Figure 9B**). As Dong Yun Shin et al. reported, the potential limiting step in formate dehydrogenation was the final step of $H_2$(g) desorption[60]. The weakest hydrogen adsorption energy over Ag/Pd (111) facet enhances hydrogen generation efficiently. And as the first step of formate adsorption, it should be a moderate to balance the adsorption rate and energy barrier of the following steps to reach a robust formate dehydrogenation. When more Ag atoms are loaded on the Pd/C surface, only the Ag atoms those form Ag/Pd structure can be involved in the dehydrogenation reaction due to the Ag/C species having no activity (**Figure 4A**). It accounts for the slightly improved hydrogen release from Pd3Ag2/ACA-G to Pd3Ag10/ACA-G. The hydrogen production comparison of Pd3Ag10/ACA-G (451 mL) and Pd3Ag10/ACA-C (301 mL) indicates the specific surface condition existing on Pd3Ag10/ACA-G is of more catalytic efficiency even though an identical Pd/Ag ratio. Firstly, as shown in TEM images (**Figure S1**), the Pd3Ag10/ACA-G has a smaller NPs size (~1.62 nm), while that of the Pd3Ag10/ACA-C sample is around 2.50 nm. The highly dispersed NPs of Pd3Ag10/ACA-G give it more chance to convert formate to bicarbonate and release hydrogen. Besides, the XPS results of Pd 3d spectra (**Figure 3A**) present that the metallic Pd 3d5/2 of Pd3Ag10/ACA-G has lower binding energies (335.7 eV) than that of Pd3Ag10/ACA-C (335.9 eV), indicating the metallic Pd over Pd3Ag10/ACA-G

has higher electronic density. As analyzed in Ag 3d spectra (**Figure 3B**), the metallic Ag atoms of Pd3Ag10/ACA-G have higher binding energies and possess higher electronic density. Combined with Pd and Ag spectra, the electron density of Pd-Ag bimetallic NPs as a whole active species is enhanced in the Pd3Ag10/ACA-G sample. According to publications, the electron-rich Pd species are more catalytic efficient for hydrogen regeneration from formate solution[10,21,60]. The hydrogen yield gradually decreases during the reusability test (**Figure 5A**), possibly because of the surface composition change. Multiple characterizations, such as XPS analysis of spent Pd3Ag10/ACA-G (**Figure 5B, C**), TEM images (**Figure 5D**), TPD (**Figure 5E**), and $^{1}H$-$^{13}C$ cross-polarization NMR (**Figure 5F**) revealed that the surface Ag fraction decrease, NPs size growth, O-containing species (carboxylate, ketones, etc.,) adsorption result in the catalyst deactivation.

## 4. Conclusion

In summary, ammonium formate solution is a promising liquid organic hydrogen carrier since both hydrogenation and dehydrogenation reactions are thermodynamically favorable, in which case hydrogen can be stored and released through the bicarbonate/formate cycles at mild conditions. However, it suffers from kinetic challenges and unclear Pd catalyst degradation mechanisms. In this report, we prepared carbon-supported Pd-Ag bimetallic NPs catalysts with two kinds of microstructures through galvanic replacement and co-reduction methods for catalyzing ammonium formate dehydrogenation. The best performed catalyst, Pd3Ag10/ACA-G, presents the highest activity with the TOF of 5202 $h^{-1}$ at 80 °C (~2.6-fold higher than 5% commercial Pd/C) and the lowest activation energy of 33.1 kJ/mol. Furthermore, the smaller NPs size, the enhanced electron density of Pd-Ag bimetallic NPs, the weakest

hydrogen adsorption energy, and intermediate formate adsorption energy over the Ag/Pd (111) facet calculated by DFT corroborate the superior formate dehydrogenation performance over the Pd3Ag10/ACA-G sample. However, changes on the catalyst surface, including surface Ag fraction decrease, NPs size growth, and O-containing species (carboxylate, ketones, etc.) adsorption, gradually deactivated the catalyst. The structural and composition parameters identified for the developed Pd-Ag bimetallic catalysts in relation to their catalytic properties towards formate dehydrogenation reaction can provide valuable guidelines for developing an efficient heterogeneous catalyst for formate-based hydrogen carrier system applications.

### CRediT authorship contribution statement

**Zhun Dong:** Conceptualization, Investigation, Writing – original draft. **Ahmad Mukhtar:** Writing – review & editing. **Thomas Ludwig:** Software, Writing – original draft. **Sneha A. Akhade:** Conceptualization, Writing – review & editing. **Wenda Hu:** Writing – original draft. **Jian Zhi Hu:** Resources, Writing – review & editing. **Katarzyna Grubel:** Validation, Writing – review & editing. **Mark Engelhard:** Resources. **Brandon C. Wood:** Resources. **Tom Autrey:** Validation, Writing – review & editing. **Hongfei Lin:** Conceptualization, Funding acquisition, Supervision, Writing – review & editing.

## Notes

The authors declare no competing financial interests.

## Acknowledgments

The authors thank for the support from the U.S. Department of Energy, Office of Energy Efficiency and Renewable Energy, Fuel Cell Technologies Office, USA (Award No. DE-EE0008826). The XPS was performed on a project award (doi:10.46936/cpcy.proj.2020.51656/60000242) from the Environmental Molecular Sciences

Laboratory, USA, a DOE Office of Science User Facility sponsored by the Biological and Environmental Research program at Pacific Northwest National Laboratory (PNNL) under Contract No. DE-AC05-76RL01830. Battelle operates PNNL for the U.S. Department of Energy. The DFT simulations were performed under the auspices of the U.S. Department of Energy by Lawrence Livermore National Laboratory, USA, under Contract DE-AC52-07NA27344. The authors acknowledge support from the Hydrogen Materials - Advanced Research Consortium (HyMARC), USA, established as part of the Energy Materials Network under the U.S. Department of Energy, Office of Energy Efficiency and Renewable Energy, Hydrogen and Fuel Cell Technologies Office. The NMR was supported by the U.S. Department of Energy, Office of Science, Office of Basic Energy Sciences (BES), Division of Chemical Sciences, Geosciences and Biosciences (Multifunctional Catalysis to Synthesize and Utilize Energy Carrier, FWP 47319).

## Reference

(1) Schlapbach, L.; Züttel, A. Hydrogen-Storage Materials for Mobile Applications. *Nature* **2001**, *414* (November), 353–358. https://doi.org/10.1038/35104634.

(2) Kumar, A.; Daw, P.; Milstein, D. Homogeneous Catalysis for Sustainable Energy: Hydrogen and Methanol Economies, Fuels from Biomass, and Related Topics. *Chem Rev* **2022**, *122* (1), 385–441. https://doi.org/10.1021/acs.chemrev.1c00412.

(3) Wei, D.; Shi, X.; Qu, R.; Junge, K.; Junge, H.; Beller, M. Toward a Hydrogen Economy: Development of Heterogeneous Catalysts for Chemical Hydrogen Storage and Release Reactions. *ACS Energy Lett* **2022**, *7* (10), 3734–3752. https://doi.org/10.1021/acsenergylett.2c01850.

(4) Alberico, E.; Nielsen, M. Towards a Methanol Economy Based on Homogeneous Catalysis: Methanol to H2 and CO2 to Methanol. *Chemical Communications* **2015**, *51* (31), 6714–6725. https://doi.org/10.1039/c4cc09471a.

(5) Asefa, T.; Koh, K.; Yoon, C. W. CO2-Mediated H2 Storage-Release with Nanostructured Catalysts: Recent Progresses, Challenges, and Perspectives. *Adv Energy Mater* **2019**, *9* (30). https://doi.org/10.1002/aenm.201901158.

(6) Bahuguna, A.; Sasson, Y. Formate-Bicarbonate Cycle as a Vehicle for Hydrogen and Energy Storage. *ChemSusChem* **2021**, *14* (5), 1258–1283. https://doi.org/10.1002/cssc.202002433.

(7) Mellmann, D.; Sponholz, P.; Junge, H.; Beller, M. Formic Acid as a Hydrogen

Storage Material-Development of Homogeneous Catalysts for Selective Hydrogen Release. *Chem Soc Rev* **2016**, *45* (14), 3954–3988. https://doi.org/10.1039/c5cs00618j.

(8) Grubel, K.; Jeong, H.; Yoon, C. W.; Autrey, T. Challenges and Opportunities for Using Formate to Store, Transport, and Use Hydrogen. *Journal of Energy Chemistry* **2020**, *41*, 216–224. https://doi.org/10.1016/j.jechem.2019.05.016.

(9) Enthaler, S.; Von Langermann, J.; Schmidt, T. Carbon Dioxide and Formic Acid - The Couple for Environmental-Friendly Hydrogen Storage? *Energy Environ Sci* **2010**, *3* (9), 1207–1217. https://doi.org/10.1039/b907569k.

(10) Koh, K.; Jeon, M.; Chevrier, D. M.; Zhang, P.; Yoon, C. W.; Asefa, T. Novel Nanoporous N-Doped Carbon-Supported Ultrasmall Pd Nanoparticles: Efficient Catalysts for Hydrogen Storage and Release. *Appl Catal B* **2017**, *203*, 820–828. https://doi.org/10.1016/j.apcatb.2016.10.080.

(11) Su, J.; Yang, L.; Lu, M.; Lin, H. Highly Efficient Hydrogen Storage System Based on Ammonium Bicarbonate/Formate Redox Equilibrium over Palladium Nanocatalysts. *ChemSusChem* **2015**, *8* (5), 813–816. https://doi.org/10.1002/cssc.201403251.

(12) Dong, Z.; Mukhtar, A.; Ludwig, T.; Akhade, S. A.; Kang, S. Y.; Wood, B.; Grubel, K.; Engelhard, M.; Autrey, T.; Lin, H. Efficient Pd on Carbon Catalyst for Ammonium Formate Dehydrogenation: Effect of Surface Oxygen Functional Groups. *Appl Catal B* **2023**, *321* (September 2022), 122015. https://doi.org/10.1016/j.apcatb.2022.122015.

(13) Hong, W.; Kitta, M.; Tsumori, N.; Himeda, Y.; Autrey, T.; Xu, Q. Immobilization of Highly Active Bimetallic PdAu Nanoparticles onto Nanocarbons for Dehydrogenation of Formic Acid. *J Mater Chem A Mater* **2019**, *7* (32), 18835–18839. https://doi.org/10.1039/c9ta06014f.

(14) Wen, M.; Mori, K.; Kuwahara, Y.; Yamashita, H. Plasmonic Au@Pd Nanoparticles Supported on a Basic Metal-Organic Framework: Synergic Boosting of H2 Production from Formic Acid. *ACS Energy Lett* **2017**, *2* (1), 1–7. https://doi.org/10.1021/acsenergylett.6b00558.

(15) Metin, Ö.; Sun, X.; Sun, S. Monodisperse Gold-Palladium Alloy Nanoparticles and Their Composition-Controlled Catalysis in Formic Acid Dehydrogenation under Mild Conditions. *Nanoscale* **2013**, *5* (3), 910–912. https://doi.org/10.1039/c2nr33637e.

(16) Nabid, M. R.; Bide, Y.; Etemadi, B. Ag@Pd Nanoparticles Immobilized on a Nitrogen-Doped Graphene Carbon Nanotube Aerogel as a Superb Catalyst for the Dehydrogenation of Formic Acid. *New Journal of Chemistry* **2017**, *41* (19), 10773–10779. https://doi.org/10.1039/c7nj01108c.

(17) Gao, S. T.; Liu, W.; Feng, C.; Shang, N. Z.; Wang, C. A Ag-Pd Alloy Supported on an Amine-Functionalized UiO-66 as an Efficient Synergetic Catalyst for the Dehydrogenation of Formic Acid at Room Temperature. *Catal Sci Technol* **2016**,

*6* (3), 869–874. https://doi.org/10.1039/c5cy01190f.

(18) Mori, K.; Dojo, M.; Yamashita, H. Pd and Pd-Ag Nanoparticles within a Macroreticular Basic Resin: An Efficient Catalyst for Hydrogen Production from Formic Acid Decomposition. *ACS Catal* **2013**, *3* (6), 1114–1119. https://doi.org/10.1021/cs400148n.

(19) Yan, J. M.; Li, S. J.; Yi, S. S.; Wulan, B. R.; Zheng, W. T.; Jiang, Q. Anchoring and Upgrading Ultrafine NiPd on Room-Temperature-Synthesized Bifunctional NH2-N-RGO toward Low-Cost and Highly Efficient Catalysts for Selective Formic Acid Dehydrogenation. *Advanced Materials* **2018**, *30* (12), 2–9. https://doi.org/10.1002/adma.201703038.

(20) Zhang, S.; Metin, Ö.; Su, D.; Sun, S. Monodisperse AgPd Alloy Nanoparticles and Their Superior Catalysis for the Dehydrogenation of Formic Acid. *Angewandte Chemie - International Edition* **2013**, *52* (13), 3681–3684. https://doi.org/10.1002/anie.201300276.

(21) Huang, Y.; Xu, J.; Ma, X.; Huang, Y.; Li, Q.; Qiu, H. An Effective Low Pd-Loading Catalyst for Hydrogen Generation from Formic Acid. *Int J Hydrogen Energy* **2017**, *42* (29), 18375–18382. https://doi.org/10.1016/j.ijhydene.2017.04.138.

(22) Tedsree, K.; Li, T.; Jones, S.; Chan, C. W. A.; Yu, K. M. K.; Bagot, P. A. J.; Marquis, E. A.; Smith, G. D. W.; Tsang, S. C. E. Hydrogen Production from Formic Acid Decomposition at Room Temperature Using a Ag-Pd Core-Shell Nanocatalyst. *Nat Nanotechnol* **2011**, *6* (5), 302–307. https://doi.org/10.1038/nnano.2011.42.

(23) Jing, H.; Wang, H. Structural Evolution of Ag-Pd Bimetallic Nanoparticles through Controlled Galvanic Replacement: Effects of Mild Reducing Agents. *Chemistry of Materials* **2015**, *27* (6), 2172–2180. https://doi.org/10.1021/acs.chemmater.5b00199.

(24) Da Silva, A. G. M.; Rodrigues, T. S.; Haigh, S. J.; Camargo, P. H. C. Galvanic Replacement Reaction: Recent Developments for Engineering Metal Nanostructures towards Catalytic Applications. *Chemical Communications* **2017**, *53* (53), 7135–7148. https://doi.org/10.1039/c7cc02352a.

(25) Especel, C.; Lafaye, G.; Epron, F. Bimetallic Catalysts for Sustainable Chemistry: Surface Redox Reactions For Tuning The Catalytic Surface Composition. *ChemCatChem* **2022**. https://doi.org/10.1002/cctc.202201478.

(26) Epron, F.; Gauthard, F.; Pinéda, C.; Barbier, J. Catalytic Reduction of Nitrate and Nitrite on Pt-Cu/Al2O3 Catalysts in Aqueous Solution: Role of the Interaction between Copper and Platinum in the Reaction. *J Catal* **2001**, *198* (2), 309–318. https://doi.org/10.1006/jcat.2000.3138.

(27) Jaegers, N. R.; Mueller, K. T.; Wang, Y.; Hu, J. Z. Variable Temperature and Pressure Operando MAS NMR for Catalysis Science and Related Materials. *Acc Chem Res* **2020**, *53* (3), 611–619. https://doi.org/10.1021/acs.accounts.9b00557.

(28) AU - Jaegers, N. R.; AU - Hu, W.; AU - Wang, Y.; AU - Hu, J. Z. High-Temperature and High-Pressure In Situ Magic Angle Spinning Nuclear Magnetic Resonance Spectroscopy. *J.Vis.Exp.* **2020**, No. 164, e61794. https://doi.org/doi:10.3791/61794.

(29) Rakita, A.; Nikolić, N.; Mildner, M.; Matiasek, J.; Elbe-Bürger, A. Re-Epithelialization and Immune Cell Behaviour in an Ex Vivo Human Skin Model. *Sci Rep* **2020**, *10* (1), 1–11. https://doi.org/10.1038/s41598-019-56847-4.

(30) Kresse, G.; Hafner, J. Ab Initio Molecular-Dynamics Simulation of the Liquid-Metalamorphous- Semiconductor Transition in Germanium. *Phys Rev B* **1994**, *49* (20), 14251–14269. https://doi.org/10.1103/PhysRevB.49.14251.

(31) Kresse, G.; Furthmüller, J. Efficiency of Ab-Initio Total Energy Calculations for Metals and Semiconductors Using a Plane-Wave Basis Set. *Comput Mater Sci* **1996**, *6* (1), 15–50. https://doi.org/10.1016/0927-0256(96)00008-0.

(32) Kresse, G.; Furthmüller, J. Efficient Iterative Schemes for Ab Initio Total-Energy Calculations Using a Plane-Wave Basis Set. *Physical Review B-Condensed Matter and Materials Physics* **1996**, *54* (16), 11169–11186. https://doi.org/10.1103/PhysRevB.54.11169.

(33) Kresse, G.; Hafner, J. Ab Initio Molecular Dynamics for Liquid Metals. *Phys Rev B* **1993**, *47* (1), 558–561. https://doi.org/10.1103/PhysRevB.47.558.

(34) Hammer, B.; Hansen, L. B.; Nørskov, J. K. Improved Adsorption Energetics within Density-Functional Theory Using Revised Perdew-Burke-Ernzerhof Functionals. *Phys Rev B Condens Matter Mater Phys* **1999**, *59* (11), 7413–7421. https://doi.org/10.1103/PhysRevB.59.7413.

(35) Joubert, D. From Ultrasoft Pseudopotentials to the Projector Augmented-Wave Method. *Phys Rev B Condens Matter Mater Phys* **1999**, *59* (3), 1758–1775. https://doi.org/10.1103/PhysRevB.59.1758.

(36) Blöchl, P. E. Projector Augmented-Wave Method. *Phys Rev B* **1994**, *50* (24), 17953–17979. https://doi.org/10.1103/PhysRevB.50.17953.

(37) Mathew, K.; Sundararaman, R.; Letchworth-Weaver, K.; Arias, T. A.; Hennig, R. G. Implicit Solvation Model for Density-Functional Study of Nanocrystal Surfaces and Reaction Pathways. *Journal of Chemical Physics* **2014**, *140* (8), 084106. https://doi.org/10.1063/1.4865107.

(38) Mathew, K.; Kolluru, V. S. C.; Mula, S.; Steinmann, S. N.; Hennig, R. G. Implicit Self-Consistent Electrolyte Model in Plane-Wave Density-Functional Theory. *Journal of Chemical Physics* **2019**, *151* (23), 234101. https://doi.org/10.1063/1.5132354.

(39) Duan, Z.; Xiao, P. Simulation of Potential-Dependent Activation Energies in Electrocatalysis: Mechanism of O-O Bond Formation on RuO2. *Journal of Physical Chemistry C* **2021**, *125* (28), 15243–15250. https://doi.org/10.1021/acs.jpcc.1c02998.

(40) Zhang, C.; Li, Y.; He, H. Sodium Promoted Pd/TiO2 for Catalytic Oxidation of Formaldehyde at Ambient Temperature. *Indoor Air 2014 - 13th International Conference on Indoor Air Quality and Climate* **2014**, 864–867.

(41) Chenakin, S. P.; Melaet, G.; Szukiewicz, R.; Kruse, N. XPS Study of the Surface Chemical State of a Pd/(SiO2 + TiO 2) Catalyst after Methane Oxidation and SO2 Treatment. *J Catal* **2014**, *312*, 1–11. https://doi.org/10.1016/j.jcat.2014.01.008.

(42) Christensen, G. L.; Langell, M. A. Characterization of Copper Palladium Oxide Solid Solutions by X-Ray Diffraction, X-Ray Photoelectron Spectroscopy, and Auger Electron Spectroscopy. *Journal of Physical Chemistry C* **2013**, *117* (14), 7039–7049. https://doi.org/10.1021/jp310344r.

(43) Tan, Y.; Wang, Y.; Jiang, L.; Zhu, D. Thiosalicylic Acid-Functionalized Silver Nanoparticles Synthesized in One-Phase System. *J Colloid Interface Sci* **2002**, *249* (2), 336–345. https://doi.org/10.1006/jcis.2001.8166.

(44) Prieto, P.; Nistor, V.; Nouneh, K.; Oyama, M.; Abd-Lefdil, M.; Díaz, R. XPS Study of Silver, Nickel and Bimetallic Silver-Nickel Nanoparticles Prepared by Seed-Mediated Growth. *Appl Surf Sci* **2012**, *258* (22), 8807–8813. https://doi.org/10.1016/j.apsusc.2012.05.095.

(45) Karatok, M.; Ngan, H. T.; Jia, X.; O'Connor, C. R.; Boscoboinik, J. A.; Stacchiola, D. J.; Sautet, P.; Madix, R. J. Achieving Ultra-High Selectivity to Hydrogen Production from Formic Acid on Pd-Ag Alloys. *J Am Chem Soc* **2023**, *145*, 5114–5124. https://doi.org/10.1021/jacs.2c11323.

(46) Zhao, X.; Xu, D.; Liu, K.; Dai, P.; Gao, J. Remarkable Enhancement of PdAg/RGO Catalyst Activity for Formic Acid Dehydrogenation by Facile Boron-Doping through NaBH4 Reduction. *Appl Surf Sci* **2020**, *512*, 145746. https://doi.org/10.1016/j.apsusc.2020.145746.

(47) Yin, B.; Zhao, E.; Hua, X.; Wang, K.; Wang, W.; Li, G.; Liu, T. Ultrafine PdAg Nanoparticles Immobilized on Nitrogen-Doped Carbon/Cerium Oxide for Superior Dehydrogenation of Formic Acid. *New Journal of Chemistry* **2020**, *44* (5), 2011–2015. https://doi.org/10.1039/c9nj05661k.

(48) Song, F. Z.; Zhu, Q. L.; Yang, X.; Zhan, W. W.; Pachfule, P.; Tsumori, N.; Xu, Q. Metal–Organic Framework Templated Porous Carbon-Metal Oxide/Reduced Graphene Oxide as Superior Support of Bimetallic Nanoparticles for Efficient Hydrogen Generation from Formic Acid. *Adv Energy Mater* **2018**, *8* (1), 1701416. https://doi.org/10.1002/aenm.201701416.

(49) Masuda, S.; Shimoji, Y.; Mori, K.; Kuwahara, Y.; Yamashita, H. Interconversion of Formate/Bicarbonate for Hydrogen Storage/Release: Improved Activity Following Sacrificial Surface Modification of a Ag@Pd/TiO2 Catalyst with a TiOx Shell. *ACS Appl Energy Mater* **2020**, *3* (6), 5819–5829. https://doi.org/10.1021/acsaem.0c00744.

(50) Bulut, A.; Yurderi, M.; Karatas, Y.; Say, Z.; Kivrak, H.; Kaya, M.; Gulcan, M.;

Ozensoy, E.; Zahmakiran, M. MnOx-Promoted PdAg Alloy Nanoparticles for the Additive-Free Dehydrogenation of Formic Acid at Room Temperature. *ACS Catal* **2015**, *5* (10), 6099–6110. https://doi.org/10.1021/acscatal.5b01121.

(51) Hu, C.; Mu, X.; Fan, J.; Ma, H.; Zhao, X.; Chen, G.; Zhou, Z.; Zheng, N. Interfacial Effects in PdAg Bimetallic Nanosheets for Selective Dehydrogenation of Formic Acid. *ChemNanoMat* **2016**, *2* (1), 28–32. https://doi.org/10.1002/cnma.201500162.

(52) Liu, H.; Huang, B.; Zhou, J.; Wang, K.; Yu, Y.; Yang, W.; Guo, S. Enhanced Electron Transfer and Light Absorption on Imino Polymer Capped PdAg Nanowire Networks for Efficient Roomerature Dehydrogenation of Formic Acid. *J Mater Chem A Mater* **2018**, *6* (5), 1979–1984. https://doi.org/10.1039/c7ta10963f.

(53) Xiao, L.; Jun, Y. S.; Wu, B.; Liu, D.; Chuong, T. T.; Fan, J.; Stucky, G. D. Carbon Nitride Supported AgPd Alloy Nanocatalysts for Dehydrogenation of Formic Acid under Visible Light. *J Mater Chem A Mater* **2017**, *5* (14), 6382–6387. https://doi.org/10.1039/c7ta01039g.

(54) Yang, L.; Hua, X.; Su, J.; Luo, W.; Chen, S.; Cheng, G. Highly Efficient Hydrogen Generation from Formic Acid-Sodium Formate over Monodisperse AgPd Nanoparticles at Room Temperature. *Appl Catal B* **2015**, *168–169*, 423–428. https://doi.org/10.1016/j.apcatb.2015.01.003.

(55) Kalinowski, H.-O.; Berger, S.; Braun, S.; Griffiths, L. *Carbon-13 NMR Spectroscopy: Wiley, Chichester, 1988 (ISBN 0-471-91306-5)*; 1989; Vol. 221. https://doi.org/https://doi.org/10.1016/S0003-2670(00)81981-9.

(56) J. Stalder, C.; Chao, S.; P. Summers, D.; S. Wrighton, M. Supported Palladium Catalysts for the Reduction of Sodium Bicarbonate to Sodium Formate in Aqueous Solution at Room Temperature and One Atmosphere of Hydrogen. *J Am Chem Soc* **2002**, *105* (20), 6318–6320. https://doi.org/10.1021/ja00358a026.

(57) Omi, H.; Ueda, T.; Miyakubo, K.; Eguchi, T. Dynamics of CO2 Molecules Confined in the Micropores of Solids as Studied by 13C NMR. *Appl Surf Sci* **2005**, *252* (3), 660–667. https://doi.org/10.1016/j.apsusc.2005.02.048.

(58) Soliman, K. A.; Kibler, L. A. Variation of the Potential of Zero Charge for a Silver Monolayer Deposited onto Various Noble Metal Single Crystal Surfaces. *Electrochim Acta* **2007**, *52* (18), 5654–5658. https://doi.org/10.1016/j.electacta.2006.12.070.

(59) Grdeń, M.; Łukaszewski, M.; Jerkiewicz, G.; Czerwiński, A. Electrochemical Behaviour of Palladium Electrode: Oxidation, Electrodissolution and Ionic Adsorption. *Electrochim Acta* **2008**, *53* (26), 7583–7598. https://doi.org/10.1016/j.electacta.2008.05.046.

(60) Shin, D. Y.; Kim, M. S.; Kwon, J. A.; Shin, Y. J.; Yoon, C. W.; Lim, D. H. Fundamental Mechanisms of Reversible Dehydrogenation of Formate on N-Doped Graphene-Supported Pd Nanoparticles. *Journal of Physical Chemistry C*

**2019**, *123* (3), 1539–1549. https://doi.org/10.1021/acs.jpcc.8b07002.